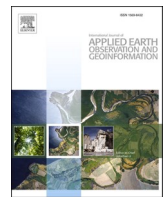




Contents lists available at ScienceDirect

International Journal of Applied Earth Observation and Geoinformation

journal homepage: www.elsevier.com/locate/jag



Fine-scale retrieval of leaf chlorophyll content using a semi-empirically accelerated 3D radiative transfer model

Xun Zhao ^{a,b}, Jianbo Qi ^{a,*}, Jingyi Jiang ^b, Shangbo Liu ^c, Haifeng Xu ^d, Simei Lin ^b, Zhexiu Yu ^b, Linyuan Li ^b, Huaguo Huang ^b

^a Faculty of Geographical Science, Beijing Normal University, Beijing 100875, China

^b State Forestry and Grassland Administration Key Laboratory of Forest Resources and Environmental Management, Beijing Forestry University, Beijing 100083, China

^c Guangzhou Institute of Forestry and Landscape Architecture, Guangzhou 510405, China

^d School of Information Science and Technology, Beijing Forestry University, Beijing 100083, China



ARTICLE INFO

Keywords:

High-resolution data
3D radiative transfer model
Retrieval
Leaf chlorophyll content

ABSTRACT

Leaf chlorophyll content (LCC) retrieval from remote sensing imagery is essential for monitoring vegetation growth and stress in the agroforestry industry. Many remote sensing inversion methods for estimating LCC primarily rely on 1D radiative transfer models (RTMs) that abstract canopies into horizontal layers or simple geometric primitives. Yet, this methodology faces challenges when applied to heterogeneous canopies, particularly in fine-scale mapping where each pixel's reflectance is significantly influenced by its surroundings, e.g. crown shadows. While 3D RTMs hold promise for addressing these challenges by explicitly describing complex canopy structures, their computational demands and the complexity involved in parameterizing detailed 3D structures limit the generation of extensive training datasets, requiring simulations across numerous parameter combinations. In this study, we used a semi-empirically accelerated 3D RTM, termed Semi-LESS, with a 1D residual network to accurately retrieve leaf chlorophyll content (LCC) from UAV images and LiDAR data at a 3-m resolution. We first reconstructed structures of forest plots using UAV LiDAR point cloud, based on which, UAV images with varying leaf and soil optical properties are simulated using the Semi-LESS. Subsequently, a training dataset consisting LCC and its corresponding reflectance was generated from the simulated UAV images by focusing on sunlit pixels. A 1D residual network is trained using the training dataset for LCC estimation. For comparison, we also trained an estimation model using a dataset generated from PROSAIL. The results show that estimation model trained with Semi-LESS surpasses PROSAIL in retrieving LCC from both simulation datasets and field measurements of two forest plots. The RMSE of Semi-LESS was 5.40–6.92 µg/cm² for simulation datasets and 8.21–9.76 µg/cm² for field measurements, whereas PROSAIL exhibited lower accuracy with an RMSE of 7.76–9.83 µg/cm² for simulation datasets and 12.76–13.06 µg/cm² in field measurements. The results demonstrate that Semi-LESS coupled with deep learning is reliable and has great potential for LCC mapping using UAV images, which is particularly useful for fine-scale applications such as crop and orchard monitoring. This approach also highlights the impact of shadows on LCC retrieval.

1. Introduction

Leaf chlorophyll content (LCC) is a key vegetation parameter for ecological models and monitoring vegetation conditions (Xu et al., 2019). As a primary photosynthetic pigment, it converts solar energy into chemical energy during photosynthesis, providing a crucial energy source for plant growth (Croft et al., 2020). The distribution of chlorophyll content is closely related to the distribution of the nutrient element nitrogen, determining the growth of vegetation crops and serving as an

important reference for implementing orchard management measures (Bhadra et al., 2024; Chen et al., 2024; Cheng et al., 2022). Additionally, chlorophyll is sensitive to various environmental stress and disturbance factors such as plant pests, drought, and nutrient deficiencies (Houborg et al., 2011; Xu et al., 2023). Hence, accurately and rapidly obtaining LCC is of significant economic and ecological value for meeting the diverse application needs of different agroforestry industries.

Traditional approaches for obtaining LCC mainly rely on field surveys or laboratory-based alcohol solvent extraction followed by

* Corresponding author.

spectrophotometric measurement (Shen et al., 2020). While these methods are capable of yielding highly accurate measurements, they necessitate the destruction of plant material and are both time-consuming and laborious (Kira et al., 2015). In contrast, remote sensing technology facilitates the acquisition of LCC by quantitatively analyzing the electromagnetic signals emitted or scattered by vegetation without the need for direct contact. This method offers unparalleled advantages for monitoring vegetation chlorophyll content on a regional and even global scale.

Although some large-scale chlorophyll products (300 m–1.15 km) are currently available (Li et al., 2021), these coarse-resolution chlorophyll products still pose an obstacle to precision agroforestry applications. On the other hand, applying traditional coarse-resolution inversion algorithms directly to high-resolution image data also poses significant challenges. This is primarily because the commonly used radiative transfer models (RTMs) like PROSAIL (Jacquemoud et al., 2009) in traditional coarse-resolution inversion algorithms usually simplify canopy as horizontal layers or simple geometric objects, making it difficult to consider heterogeneous canopy structures (Ferreira et al., 2018), especially at fine spatial scales. In particular, the reflectance of a high-resolution pixel is easily affected by surrounding vegetation canopies, including crown shadowing and multiple scattering (Chen and Leblanc, 2001). Consequently, there is an urgent need for a radiative transfer model that can accurately describe the interaction between solar radiation and the complex forest canopy, facilitating fine-scale and accurate LCC retrieval. Fortunately, 3D RTMs that considers explicit canopy structures offer a potentially viable solution to this requirement.

Currently, several 3D RTMs have been developed, such as DART (Gastellu-Etchegorry et al., 2004), LESS (Qi et al., 2019), FLIGHT (North, 1996) and RAPID (Huang et al., 2013). These models have also been extensively utilized across a spectrum of applications, including sensitivity analysis of remote sensing signals (Liu et al., 2019), inversion algorithm evaluation (Lin et al., 2024), physical model validation (Bian et al., 2022), and sensor performance assessment (Zhao et al., 2023). Nevertheless, there remains a paucity of research that directly applies these 3D RTMs to the inversion of vegetation parameters, compared with simplified 1D radiative transfer models. The primary challenges encompass the difficulty in obtaining accurate 3D structural information of vegetation and the relatively low computational efficiency associated with 3D radiative transfer simulations (Li et al., 2021). These factors pose difficulties in fulfilling the simulation requirements for datasets, particularly under the constraints of a multitude of diverse parameter combinations in inversion applications.

With the advancement of LiDAR technology, it has garnered widespread attention due to its capability to acquire high-precision 3D structural information (Coops et al., 2021). Consequently, an increasing number of researchers are leveraging LiDAR to supply accurate structural data, which serves as input for parameterizing 3D RTMs (He et al., 2024; Zhao et al., 2024). However, the growing volume of 3D data increases the computational complexity, necessitating an enhancement of 3D radiative transfer modeling to achieve greater efficiency. Several approaches have been proposed to tackle this challenge by using techniques such as octree acceleration data structure (Li et al., 2018) or hardware acceleration methods like Graphics Processing Unit (GPU) (Bailey, 2014). Additionally, semi-empirical methods that combine traditionally analytical radiative transfer equations with modern 3D radiative transfer simulations have also been explored (Jiang et al., 2020). For example, (Qi et al., 2023) introduced a semi-empirically accelerated 3D radiative transfer modeling approach termed Semi-LESS, which is capable of analytically and accurately computing canopy reflectance under arbitrary combinations of leaf biochemical parameters and soil backgrounds across different wavelengths. It achieves this with minimal computational overhead, requiring only a single LESS simulation for a specified canopy configuration. Compared with the use of LESS alone for reflectance simulations, the Semi-LESS achieves a 320-fold increase in computational efficiency. Furthermore, using the

benchmark scenes provided by the RADiation transfer Model Inter-comparison (RAMI) initiative, Semi-LESS has demonstrated exceptionally high accuracy, with a root mean square error (RMSE) of less than 0.0003 (Qi et al., 2023). This level of precision and efficiency significantly enhances the potential for accurately estimating vegetation biochemical parameters through the efficient simulation of remote sensing signals using 3D RTMs.

Based on the preceding analysis, this study proposes an approach that integrates LiDAR technology with the Semi-LESS model to facilitate fine-scale estimation of leaf chlorophyll content (LCC) in heterogeneous canopies—a task that often poses challenges for conventional and simplified radiative transfer models. Specifically, unmanned aerial vehicle (UAV) LiDAR data is first used to construct 3D scenes, and then a simulation dataset was generated with the Semi-LESS model. The training dataset was then input into a 1D residual network to train the neural network, and fine-scale retrieval of LCC was conducted using observed UAV images. The materials and methods are described in Section 2. Results are displayed in Section 3, and discussions are presented in Section 4, with conclusions summarized in Section 5.

2. Material and methods

2.1. Study area

The study area (Fig. 1e) is situated within the Saihanba Forest Farm (SFF) in Weichang County, Hebei Province, China. The SFF is one of the largest plantation forests in China. The forest vegetation mainly comprises Larch (*Larix principis-rupprechtii*), Spruce (*Picea asperata*), and mixed forests, with Larch being the predominant species covering an area of approximately 72,000 ha, which accounts for 70 % of the total planted area. In the study area, two plantation plots were selected: a Larch plot (50 m × 50 m) (Fig. 1a) and a Spruce plot (20 m × 30 m) (Fig. 1c).

2.2. Dataset

2.2.1. Field measurements

During July 22 to 23, 2022, due to high labor costs, we randomly selected a portion of tree samples from the Larch and Spruce plots for measuring leaf chlorophyll content (LCC). Ultimately, 28 trees were selected from the Larch plot and 17 trees from the Spruce plot. Nine leaves were collected from each sampled tree at different heights and orientations to reduce LCC distribution variability. It should be noted that due to the inaccessibility of the upper canopy, leaves from the highest tree regions were not sampled. Each leaf sample was then placed in plastic bags and labeled with a tree ID. The coordinates of sampled trees were also recorded using handheld GPS devices. After collecting the leaves, a digital hemispherical photography camera was used to capture hemispherical images for obtaining canopy coverage of each plot. Subsequently, the collected leaves were promptly brought back to the laboratory for chlorophyll content measurement using Chlorophyll Content Meter (CCM-300). Specifically, we first connected the optical fiber probe to the CCM-300 device using two threaded connections, then attached the other end of the fiber to the leaf clip to measure the LCC of the collected pine needles. For each needle, we selected two positions for measurement and recorded the corresponding readings. Using this method, we measured all leaf samples collected from each tree (2 measurement positions per needle * 9 needle samples = 18 measurements). Finally, the average LCC of each tree was represented by the mean value of the 18 measurements. The hemispherical images were further segmented to obtain canopy coverage by using CAN-EYE (French National Institute of Agronomical Research, INRAE), with the Larch and Spruce plots having canopy coverages of 0.62 and 0.42, respectively.

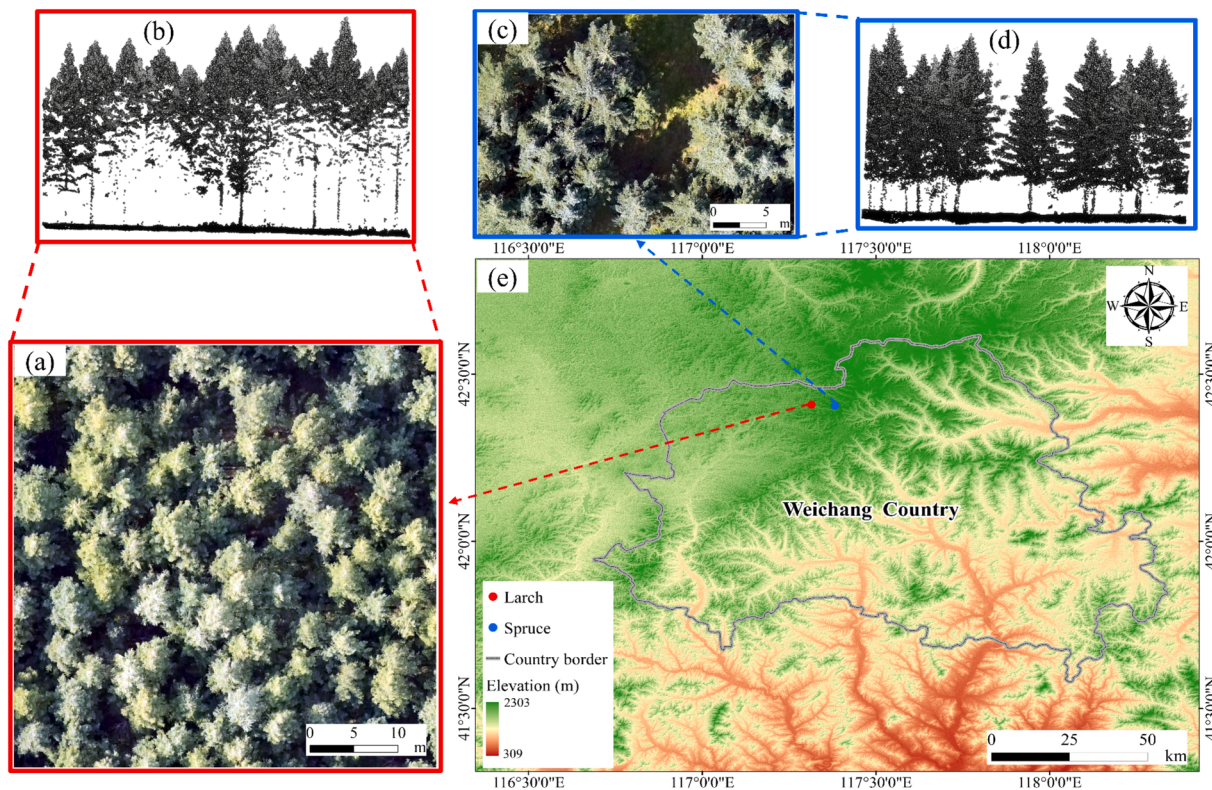


Fig. 1. Study area and selected forest plots: (e) the locations of the two selected forest plots; (a)–(b) the UAV RGB image and LiDAR point cloud of the Larch plot; (c)–(d) the UAV RGB image and LiDAR point cloud of the Spruce plot.

2.2.2. UAV LiDAR data and images

The unmanned aerial vehicle (UAV) LiDAR data was acquired on July 21st, 2022 with a Rigel miniVUX-1UAV LiDAR sensor (**Table 1**) mounted on a quadcopter UAV. Considering the local terrain elevation and canopy height of the two plots, a flight altitude of 50 m was set for acquiring the LiDAR data. This yields a point cloud density of approximately 2000 pts/m² (**Table 2**). Subsequently, the boundaries of the two plots measured with GPS were used to clip the point clouds, providing a foundational dataset for reconstructing 3D forest scenes.

The UAV multispectral imagery data was acquired on July 30th, 2022, with a DJI Phantom 4 Multispectral quadcopter platform (**Table 1**), which consists of an RGB camera and a five-band multispectral camera. The flight missions for the two plots were conducted around noon to ensure direct sunlight dominated the total radiation, with the solar zenith angle and azimuth angle further calculated based on the plots' positions, altitude and flight time. Two different flight altitudes of 75 m and 50 m was employed for the UAV multispectral imagery data flights over the Larch and Spruce plots, resulting in extremely high spatial resolution images (<= 4 cm). More detailed information about

the data is presented in **Table 2**. Subsequently, a reference panel with a reflectance of 0.5 and three reference cloths with reflectance of 0.2, 0.4, and 0.6 were used for calibrating the acquired UAV multispectral imagery reflectance. Photos alignment, image stitching and orthophoto generation were performed with the Metashape (©Agisoft LLC). After the image processing, each individual tree crown was manually delineated based on field surveys of individual tree locations for validation of LCC retrieval. Finally, to complete the registration between the images and the point cloud, we generated the photogrammetric point cloud after photo alignment to reduce errors from directly registering the two different data modalities. Specifically, using the photogrammetric point cloud as a reference, we applied the ICP algorithm (Gressin et al., 2013) to align the airborne LiDAR data to the UAV photogrammetric point cloud. Furthermore, using the registered ALS point cloud as a reference, we manually fine-tuned the UAV images based on corresponding tree crown top points to achieve pixel-level precise alignment between the UAV images and the ALS point cloud.

2.3 Overview of the LCC retrieval algorithm

The technical flowchart for fine-scale retrieval of LCC is presented in **Fig. 2**, which primarily consists of 5 steps: 1) reconstructing 3D explicit forest scenes based on acquired UAV point cloud data; 2) fast simulation of multispectral images with different soil optical properties and leaf biochemical parameters including LCC; 3) training a residual network-based LCC inversion model, using the simulated multispectral images and the corresponding LCC; 4) performing fine-scale LCC retrieval using real UAV images as input for the LCC retrieval model. 5) evaluating the estimated LCC with both simulated data and field-measured LCC.

2.4. Reconstructing forest scenes from UAV point cloud

UAV point cloud data of the two selected forest plots was utilized to reconstruct detailed 3D forest scenes by employing the 3D

Table 1

The device parameters of the UAV sensors.

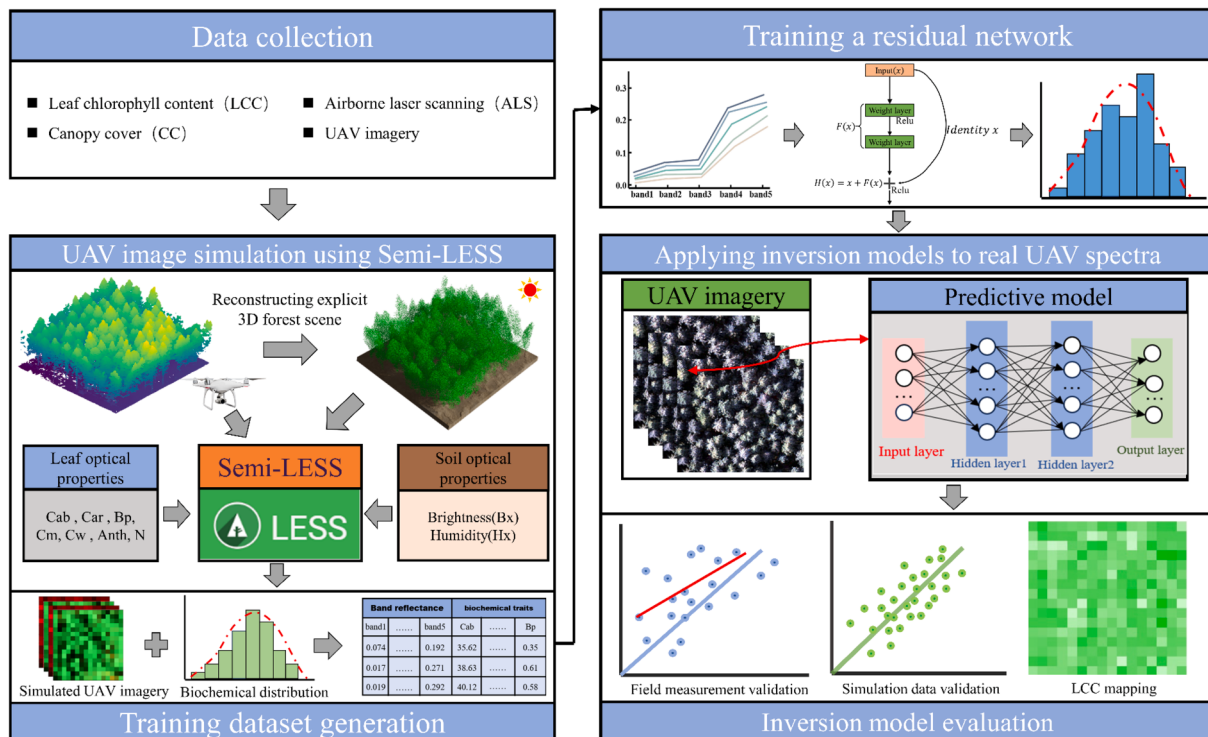
Sensor Types	Parameters	Values
LiDAR	Pulse frequency	100 KHZ
	Pulse divergence angle	1.6 × 0.5 mrad
	Range accuracy	15 mm
	Wavelength	905 nm
Multispectral	Band1 (Blue)	450 nm ± 16 nm
	Band2 (Green)	560 nm ± 16 nm
	Band3 (Red)	650 nm ± 16 nm
	Band4 (Red edge)	730 nm ± 16 nm
	Band5 (Near-infrared)	840 nm ± 26 nm
	FOV	62.7°
	Focal length	5.74 mm

Table 2

The parameters of the acquired UAV data.

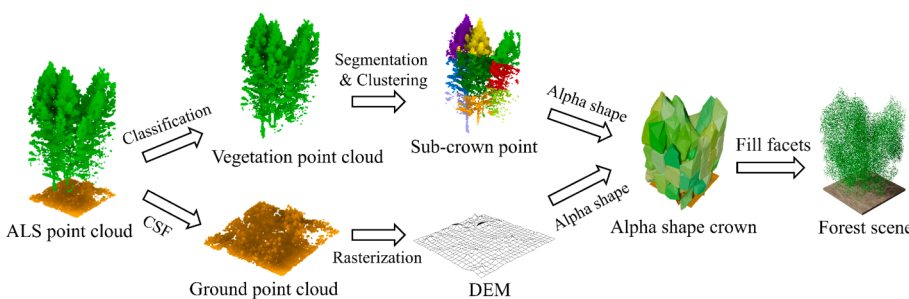
Data types	Plot	Date	SAA	SZA	Flight Height	Point density	Resolution
LiDAR	Larch& Spruce	2022,7,21	—	—	50 m	2000 pts/m ²	—
Multispectral	Larch	2022,7,30	266.32°	58°	75 m	—	4 cm
	Spruce		242.81°	38.53°	50 m	—	2.6 cm

Note: SAA is Solar Azimuth Angle, SZA is Solar Zenith Angle.

**Fig. 2.** Leaf chlorophyll content (LCC) retrieval technique flowchart.

reconstruction module (Fig. 3) provided by the 3D RTM LESS (Qi et al., 2022, 2017). LESS is a state-of-the-art 3D RTM that can simulate various remote sensing signals by configuring different sensor parameters, providing a reliable foundation for the development and validation of remote sensing models and retrieval algorithms (Zeng et al., 2023). It has been compared and validated against international radiative transfer model benchmark scenarios (Widłowski et al., 2015), demonstrating comparable accuracy to reference values. Within the 3D reconstruction module of LESS, a ground filtering algorithm, named cloth simulation filtering algorithm (CSF) (Zhang et al., 2016), was initially applied to classify the point clouds into ground and non-ground points. The ground points were then rasterized to generate a digital elevation model (DEM) and input into LESS to generate the terrain of the plots. Subsequently, the non-ground points were segmented into sub-crown using a

combination of the watershed segmentation and the k-means clustering algorithm (Qi et al., 2022). To account for the vertical heterogeneity of tree crowns, the non-ground points were further evenly divided into three layers. Combining the segmented sub-crown point clouds, we reconstructed the geometric contours of each sub-crown using a 3D alphashape method (Edelsbrunner and Mücke, 1994). Based on the reconstructed alphashape crowns and the intensity information of each sub-crown point cloud, we employed a path length distribution algorithm (Gao et al., 2023) to estimate the Plant Area Index (PAI) for the purpose of parameterizing each sub-crown. Finally, based on the estimated PAI values, each sub-crown was filled with randomly distributed rectangular facet with a size of 0.01 m², and the leaf angle distribution was set as spherical.

**Fig. 3.** The process of reconstructing 3D forest scenes from ALS data.

2.5. UAV image simulation using Semi-LESS

2.5.1. Semi-LESS

UAV images can be rapidly simulated using Semi-LESS (Fig. 4). According to (Jiang et al., 2020; Qi et al., 2023), The relationship between soil background and the canopy reflectance can be analytically computed as:

$$R = \rho_{so} + r \frac{T_1 - r\rho_{dd}T_2}{1 - r\rho_{dd}} \quad (1)$$

where R is canopy reflectance, ρ_{so} is the canopy reflectance with a black soil, ρ_{dd} is the bihemispherical reflectance, r is soil reflectance, $T_1 = \tau_{ssoo} + \tau_{ss}\tau_{do} + \tau_{sd}\tau_{do} + \tau_{sd}\tau_{oo}$ and $T_2 = \tau_{ssoo} + \tau_{ss}\tau_{oo}$ are different combinations of canopy transmittance. Here, the subscript s is the light source direction, o is the observation direction, and d is the downward or upward diffuse direction. τ_{ssoo} is the bidirectional gap probability. Although equation (1) provides an analytical solution describing the quantitative relationship between canopy reflectance and properties, including soil reflectance and canopy transmittance. However, for a heterogeneous 3D scene, these unknown quantities cannot be computed directly. Instead of solving analytically, we used LESS simulations to compute the S term ($S = [\rho_{so}, \rho_{dd}, T_1, T_2]$) by using four reference soil values ($[r_0, r_1, r_2, r_3]$). Subsequently, the dependence of $[\rho_{so}, \rho_{dd}, T_1, T_2]$ on leaf biochemical composition and wavelength is achieved by a curve fitting. Specifically, for a given leaf mesophyll structure parameter N , canopy structure and observation geometry, the variation of each quantity of $[\rho_{so}, \rho_{dd}, T_1, T_2]$ can be well described with a smooth function dependent on the total leaf absorption coefficient K . In this study, we set N to 1.5, which satisfies the reflectance simulation for different vegetation types (Jiang et al., 2020; Qi et al., 2023). Furthermore, fourteen K values covering the variations from 400 nm to 2200 nm was used to make the curve. Finally, these parameters require a combination of $4 \times 14 = 56$ simulations to calibrate equation (1). However, we can combine them into a 56-channel multispectral image, which requires only a single LESS simulation. In total, the above procedure provides a solution to efficiently simulate canopy reflectance images under arbitrary combinations of leaf and soil optical properties, with a pre-simulated coefficient image, i.e., the 56-channel multispectral image (Fig. 4).

2.5.2. UAV image simulation

We utilized the reconstructed forest scenes of the Larch and Spruce plots from UAV point cloud data, as detailed in Section 2.4, to simulate UAV images. We separately configured the solar zenith angles and azimuth angle for the two plots derived from UAV data flight times and conducted coefficient image simulations using the Semi-LESS model. The spatial resolution of the coefficient image simulations was configured to match the 4 cm and 2.6 cm resolutions of the observed UAV imagery in the Larch and Spruce plots, respectively. In conjunction with the simulated coefficient images, different combinations of biochemical parameters were input into Semi-LESS for multispectral image simulation, including the blue, green, red, red edge and near-infrared bands.

Specifically, since reflectance in the visible and near-infrared spectral ranges is insensitive to leaf water content and anthocyanin (Cheng et al., 2022), we fixed leaf water content (C_w) at 0.015 and anthocyanin (C_{anth}) at 0. Other biochemical parameters, including chlorophyll content (C_{ab}), brown pigment content (C_{bp}), dry matter content (C_m), and leaf structural parameter (N), were sampled within specified range and increments as detailed in Table 3. Due to the stable relationship between chlorophyll and carotenoids, a ratio of 4:1 was employed to set the carotenoid values (Li et al., 2022). To simulate a more continuous distribution of biochemical parameters, a random gaussian distribution function, with a mean of 0 and a standard deviation half of each biochemical parameter step value, was applied to each original value of the biochemical parameters, according to equation (2):

$$P_{bio}^* = P_{bio} + \text{random}(N(0, S_{bio}/2)) \quad (2)$$

where P_{bio}^* represents biochemical parameter (e.g., C_{ab} , C_{bp} , C_m , N) obtained by adding each original biochemical parameter P_{bio} sampled with uniform interval steps with a randomly sampled value, S_{bio} represents the step size for sampling each different biochemical parameter, $\text{random}(N(0, \sigma))$ is a random gaussian normal distribution function with a mean of 0 and a standard deviation of σ . The final generated P_{bio}^* is also constrained within the minimum and maximum range values of each parameter (e.g., $C_{ab,min} \leq P_{C_{ab}}^* \leq C_{ab,max}$). For soil reflectance, the GSV soil model was coupled to obtain different soil reflectance values (Jiang and Fang, 2019). The brightness and humidity of the soil were uniformly sampled within the ranges of [0.01, 0.7] and [0.01, 0.78] using a uniform distribution function, respectively. Finally, all these combinations of parameters are input into the Semi-LESS model to simulate UAV imagery.

2.6. Training dataset generation

2.6.1. Dataset generated from simulated UAV images

To generate the training dataset from the simulated UAV images, a pixel threshold of 25 % reflectance in the NIR (840 nm) band was used to select only sunlit pixels (Ferreira et al., 2018). Specifically, for each simulated multispectral image, the near-infrared band was initially utilized to generate a mask band, labeling sunlit pixels (with reflectance $>25\%$) as 1 and shadow pixels (with reflectance $\leq 25\%$) as 0. This mask band was then applied to its corresponding simulated multispectral image through multiplication to isolate the sunlit pixels. Subsequently, the images with only sunlit pixels were aggregated into 3 m resolution images. The 3 m resolution is chosen because it is comparable with average crown size in this area, facilitating the validation, and are more suitable for LCC retrieval than original 2.6 or 4 cm resolutions. We further processed each new multispectral image by iterating through each pixel to obtain the multi-spectral reflectance and corresponding LCC values. This process generated a comprehensive training dataset with a size of 182,560 entries.

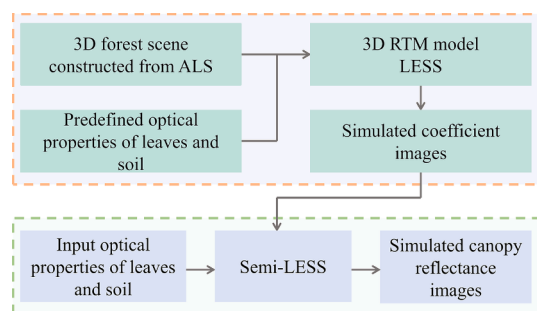


Fig. 4. Semi-LESS simulated multispectral image workflow diagram.

Table 3
The main parameter settings of the Semi-LESS and PROSAIL model.

Type	Parameter	Avg	SD	Min	Max	Step
Leaf	N	1.7	0.4	1	2.5	0.5
	$C_{ab}(\mu\text{g}/\text{cm}^2)$	39.9	10.8	10	70	10
	$C_{ar}(\mu\text{g}/\text{cm}^2)$	9.9	2.7	2.5	17.5	—
	$C_m(\text{g}/\text{cm}^2)$	0.015	0.008	0	0.03	0.01
	$C_w(\text{cm})$	0.015	—	—	—	—
	C_{bp}	0.4	0.23	0	0.8	0.2
	$C_{anth}(\mu\text{g}/\text{cm}^2)$	0	—	—	—	—
	B_s	0.35	0.20	0.01	0.7	—
Soil	H_s	0.38	0.22	0.01	0.78	—

2.6.2. Dataset generated from PROSAIL for comparison

Furthermore, to compare the fine-scale leaf chlorophyll content (LCC) retrieval capabilities of Semi-LESS and the 1D RTM PROSAIL, the PROSAIL model, which couples the leaf-level radiative transfer model (RTM) PROSPECT (Feret et al., 2008) with the canopy-level RTM SAIL (Verhoef, 1984), was also used to simulate UAV spectral reflectance. Specifically, the leaves and soil parameters input into the PROSAIL model were kept consistent with those of the Semi-LESS model (Table 3). The leaf angle distribution function was also set to a spherical distribution. For the canopy leaf area index (LAI) values, we parameterized the PROSAIL model using the PAI inverted from UAV point cloud data. Specifically, for the reconstructed Larch and Spruce plots described in Section 2.4, the PAI values with 3-m resolution were calculated and input into the PROSAIL model (Fig. 5). Finally, different solar zenith angles and azimuth angles from Table 2 were used to simulate canopy reflectance. The detailed information of model parameters for Semi-LESS and PROSAIL is presented in Table 3.

2.7. LCC retrieval using residual network

We use residual networks to estimate LCC in this study. Residual networks primarily incorporate residual blocks, which enable direct transmission of input information from preceding layers to subsequent output layers through shortcuts or skip connections. This approach allows for increased network depth, improves training capacity, and mitigates the vanishing gradient problem associated with deep networks (Makhlofi and Kallel, 2023).

The residual network architecture we employ is illustrated in Fig. 6. The network primarily comprises six hidden layers, with the neuron counts of the first three hidden layers being 800, 400, and 200, respectively. The remaining three hidden layers are embedded within a residual block. Specifically, the output of the third hidden layer is directly connected to the last hidden layer through a residual block. Moreover, the Sigmoid activation function is utilized in the final layer of the network, the ReLU activation function is applied to the rest of the layers to better fit nonlinear relationships. An Adam optimizer with a learning rate of 0.001 is employed to better adjust the network parameters and minimize the loss function for retrieval leaf chlorophyll content, and a weight decay coefficient of 0.001 was set to prevent network overfitting. An MSE function is used to measure the difference between the network's predicted values and the observed values of LCC. Finally, Simulated datasets from two different plots, generated using the Semi-LESS and PROSAIL models, are randomly divided into two subsets: an 80 % training set for training the residual network, and a separate 20 % testing set derived from each plot. These testing sets are utilized to independently assess the model's accuracy across the different plots.

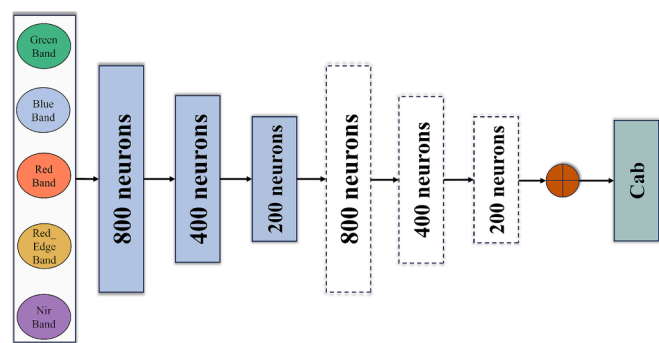


Fig. 6. Residual network architecture.

2.8. Evaluation of accuracy

We evaluated the accuracy of the residual network's LCC retrieval model using the remaining 20 % of datasets from different plots and RTMs, and field measurement. For the field measurement-based evaluation, UAV multispectral images are initially filtered to select sunlit pixels as detailed in Section 2.6. Subsequently, these selected sunlit pixels are aggregated into 3 m multispectral images, and the multispectral reflectance of each pixel is then extracted as input for the residual network to predict LCC. Furthermore, measured single-tree LCC values are employed to assess the accuracy of the LCC model. However, during the evaluation process, each single-tree canopy may be contained within a single pixel or span multiple pixels. To minimize bias in LCC extraction, we processed each tree canopy individually. For canopies fully within a pixel, we used that pixel's value as the predicted LCC. For canopies spanning multiple pixels, we determined the proportion of the canopy over each pixel, applied it to the weighted pixel values, and calculated the predicted LCC. The model's accuracy was then assessed using root mean square error (RMSE), relative root mean square error ($rRMSE$), and coefficient of determination (R^2).

3. Results

3.1. Visualization of sunlit and shadow pixels

The visualization of sunlit and shadowed pixel areas in the Larch and Spruce plots is shown in Fig. 7. It can be observed that applying a NIR reflectance threshold of 25 % to the original multi-band images (Fig. 7 (a, c)) enables the differentiation of sunlit and shadow pixels (Fig. 7 (b, d)). Based on the selected pixels, the corresponding average spectral reflectance curves for sunlit, shadow, and all pixels of each plot are also visualized in Fig. 8(a, b). It is observed that the overall average spectral reflectance of sunlit pixels is significantly higher compared to that of the

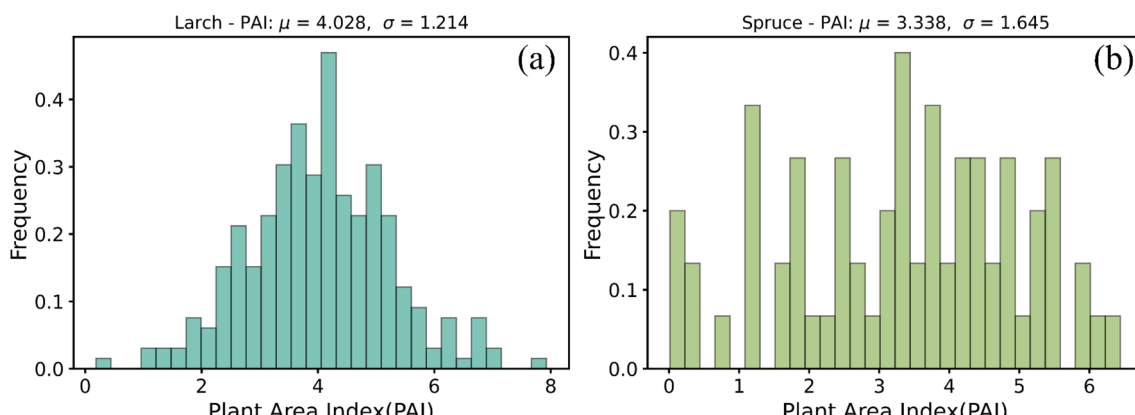


Fig. 5. The estimated PAI distribution from UAV point clouds for the Larch (a) and Spruce (b) plot.

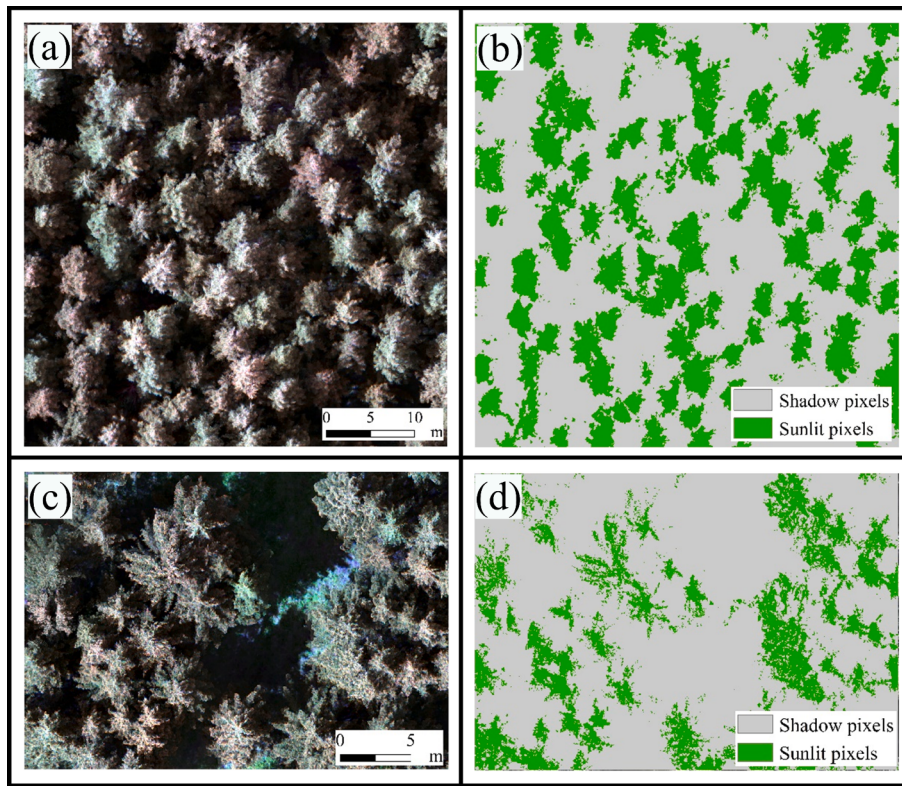


Fig. 7. The visualization displays the differentiated areas of sunlit and shadowed pixels based on the near-infrared band reflectance threshold. ((a) and (c) show RGB images comprised of multi-band UAV imagery from the Larch and Spruce plots, respectively. (b) and (d) depict corresponding segmented sunlit and shadowed pixel areas for each plot.).

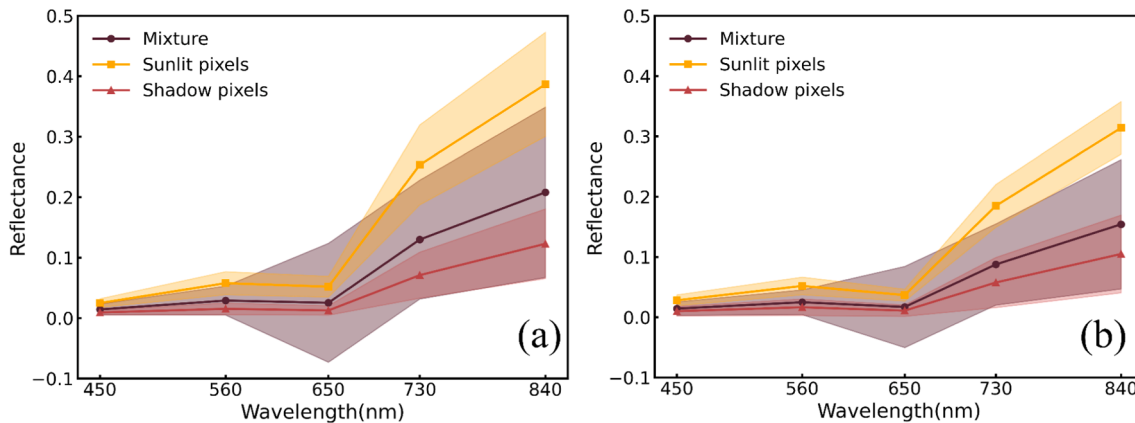


Fig. 8. Comparison of average spectral reflectance curves for mixed sunlit and shadow pixels, as well as distinct sunlit and shadow pixels in (a) Larch and (b) Spruce plots.

shadowed pixels. Furthermore, compared to the average spectral reflectance curves made by mixing all pixels, the curves for sunlit pixels exhibit more pronounced features in pigment-related bands, such as the green band.

3.2. Evaluating realism of UAV reflectance simulations

The relationship between the simulated UAV reflectance by Semi-LESS and PROSAIL and the observed UAV reflectance in different bands, as well as the comparison of the distribution of each band, are presented in Fig. 9. It can be observed that the simulated UAV reflectance from Semi-LESS (Fig. 9 (a)) and PROSAIL (Fig. 9 (b)) exhibits similar distributions. Furthermore, based on the extensive input

parameters (Table 3) of the Semi-LESS and PROSAIL model as described in Section 2.5, scatter plots indicate that the datasets generated by the two simulation models, Semi-LESS (Fig. 9 (a)) and PROSAIL (Fig. 9 (b)), still adequately encompass the range of observed UAV reflectance data. The correlation values calculated from the two simulated datasets indicate poor correlation between the red-edge and near-infrared bands with the reflectance in different bands of the visible spectral range (excluding the green band). This result is consistent with the correlation results obtained from the observed UAV reflectance. The presentation of the distributions and correlation coefficients of these different bands also indicates that these simulated UAV datasets can be effectively used for subsequent LCC retrieval.

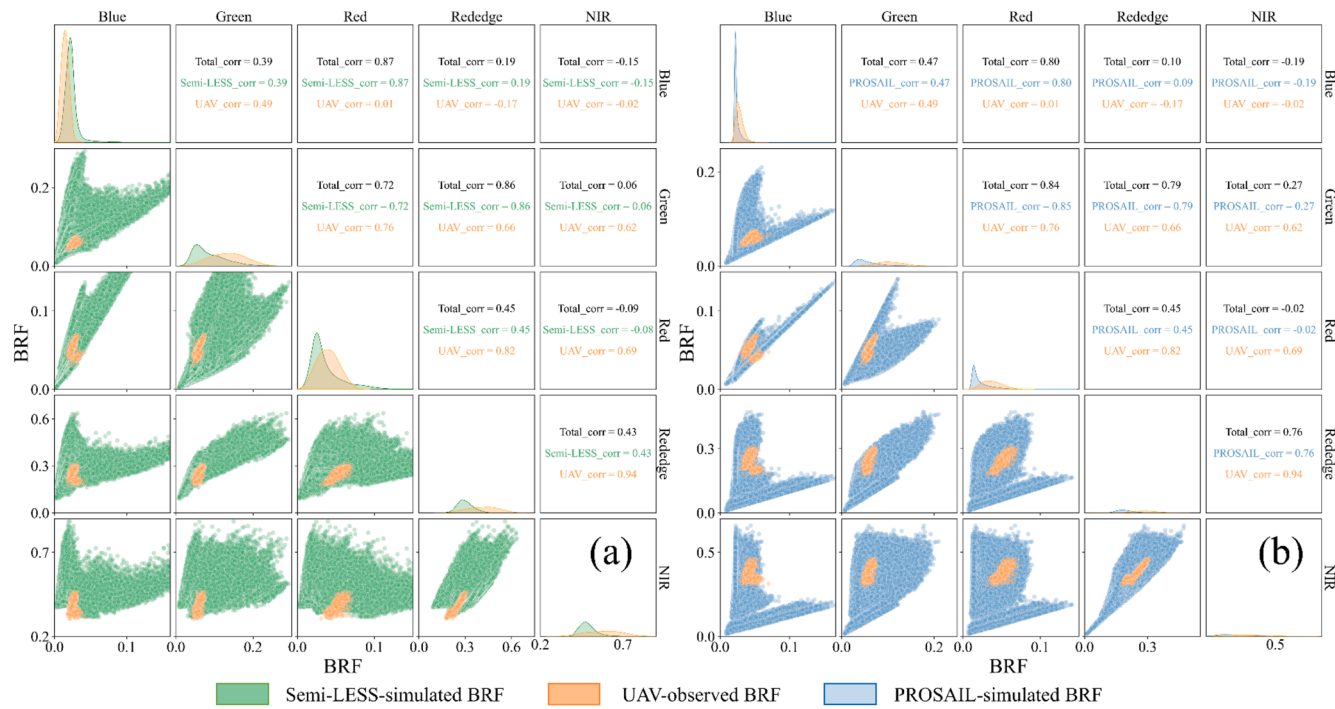


Fig. 9. Comparing the relationship between simulated UAV reflectance using Semi-LESS (a) and PROSAIL (b) models and observed UAV reflectance.

3.3. Accuracy comparison

Residual networks trained on Semi-LESS dataset and PROSAIL dataset were evaluated for their retrieving accuracy. For the Semi-LESS dataset, to compare the impact of shadows on LCC retrieval, simulated reflectance datasets with and without shadows were employed, respectively. Table 4 compares the accuracy of residual network LCC retrieval using 20 % simulated datasets from different plots and RTMs. It can be observed that when using the Semi-LESS dataset for neural network training, in the case of Larch plot, simulated data testing samples show a significant increase in the accuracy of LCC retrieval before and after shadow exclusion. Specifically, the coefficient of determination (R^2) for LCC retrieval by the model increased from 0.87 to 0.91, the root mean square error (RMSE) decreased from $6.7 \mu\text{g}/\text{cm}^2$ to $5.4 \mu\text{g}/\text{cm}^2$, and the relative root mean square error ($rRMSE$) remained unchanged at 0.001. In the case of Spruce plot, simulated data testing samples show a similar trend in the accuracy of LCC retrieval before and after shadow exclusion, with R^2 increasing from 0.76 to 0.86, RMSE decreasing from $9.08 \mu\text{g}/\text{cm}^2$ to $6.92 \mu\text{g}/\text{cm}^2$, and $rRMSE$ decreasing from 0.003 to 0.002. In comparison, when using PROSAIL dataset simulated data for neural network training, in the case of Larch plot, the R^2 is 0.81, RMSE is $7.76 \mu\text{g}/\text{cm}^2$, and $rRMSE$ is 0.001. in the case of Spruce plot, R^2 is 0.7, RMSE is $9.83 \mu\text{g}/\text{cm}^2$, and $rRMSE$ is 0.004. Overall, the accuracy of LCC retrieval models is superior when trained on the Semi-LESS simulated data compared to the accuracy of models trained on the PROSAIL simulated data. Meanwhile, the simulated data

indicate that the accuracy of LCC retrieval for the Larch plot is higher than that for the Spruce plot.

To further assess the model's applicability to field-measurement data, 1D residual networks trained on simulated datasets generated by both the Semi-LESS and PROSAIL models were also executed for accuracy comparison at two selected plots. The accuracy of LCC retrieval for the Semi-LESS model, both before and after shadow exclusion, is presented in Fig. 10. It can be observed that in the case of Larch plot, the R^2 accuracy of the network's LCC retrieval increased from 0.33 before (Fig. 10 a) shadow exclusion to 0.42 after (Fig. 10 b), with the RMSE and $rRMSE$ decreased from $10.68 \mu\text{g}/\text{cm}^2$ and 0.07 to $8.21 \mu\text{g}/\text{cm}^2$ and 0.05, respectively. Similarly, in the case of Spruce plot, R^2 increased from 0.29 before shadow exclusion (Fig. 10 c) to 0.33 after (Fig. 10 d), and both RMSE and $rRMSE$ decreased from $11.51 \mu\text{g}/\text{cm}^2$ and 0.1 to $9.76 \mu\text{g}/\text{cm}^2$ and 0.09, respectively. Additionally, for comparison, the accuracy of LCC retrieval for the PROSAIL model is presented in Fig. 11. It can be observed that the accuracy of LCC retrieval by the residual network for the Larch plot is $R^2 = 0.16$, RMSE = $12.76 \mu\text{g}/\text{cm}^2$, $rRMSE = 0.09$, whereas for the Spruce plot, it is $R^2 = 0.26$, RMSE = $13.06 \mu\text{g}/\text{cm}^2$, $rRMSE = 0.1$. Overall, whether for the Larch or Spruce plot, the accuracy of LCC retrieval by residual networks trained on the Semi-LESS dataset (Fig. 10) is superior to that of models trained on the PROSAIL dataset (Fig. 11). The performance on different plots indicates that the accuracy of LCC retrieval by models trained on both the Semi-LESS dataset and PROSAIL dataset is higher for the Larch plot compared to the Spruce plot. These results are consistent with those presented by the simulated

Table 4

Comparing the accuracy of residual network LCC retrieval using 20% different simulated dataset models (Semi-LESS dataset and PROSAIL dataset) from the Larch and Spruce plots.

Dataset	Description	Larch R^2	RMSE ($\mu\text{g}/\text{cm}^2$)	$rRMSE$	Spruce R^2	RMSE ($\mu\text{g}/\text{cm}^2$)	$rRMSE$
Semi-LESS dataset	Including shadows	0.87	6.70	0.001	0.76	9.08	0.003
	Excluding shadows (Nir > 25 %)	0.91	5.40	0.001	0.86	6.92	0.002
PROSAIL dataset	Including shadows	0.81	7.76	0.001	0.70	9.83	0.004

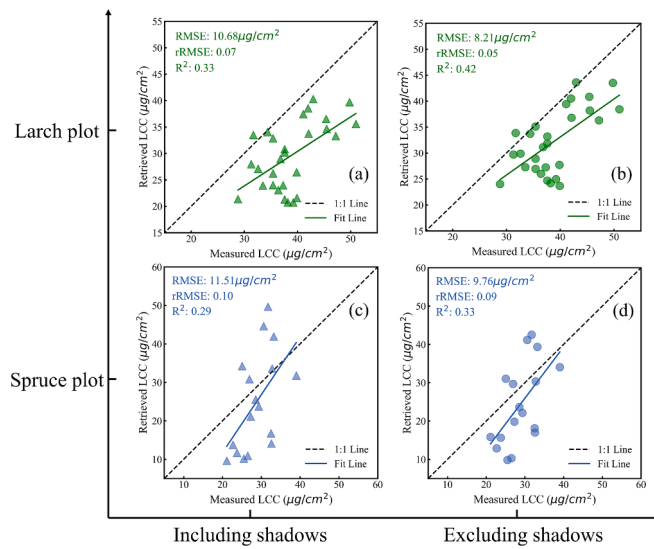


Fig. 10. The comparison of LCC retrieval accuracy by residual networks before (a, c) and after (b, d) shadow exclusion in the Larch and Spruce plots (Residual networks trained based on the Semi-LESS dataset).

dataset (Table 4).

4. Discussion

4.1. Estimation accuracy

In this study, we employed a semi-empirically accelerated 3D RTM, Semi-LESS, coupled with a 1D residual network to retrieval fine-scale LCC. Utilizing Semi-LESS, we can efficiently simulate fine-scale UAV reflectance and generate a training dataset for training deep learning LCC retrieval models. At the same time, test datasets derived from theoretical simulation data and field-measured LCC data show that our proposed method can accurately produce fine-scale LCC inversion results. However, when compared to previous studies on the retrieval of LCC parameters, the R² and RMSE-based accuracy assessment of our field measurements shows that the precision of LCC retrieval remains suboptimal. This limitation primarily arises from the fact that previous studies were predominantly conducted on homogeneous crops or structurally simple orchards, which present a less complex challenge for LCC retrieval (Bhadra et al., 2024; Makhlofi and Kallel, 2023; Zhang et al., 2024). In contrast, our study tackles the intricate structures of forests, where the reflectance of each pixel is more susceptible to

influence from surrounding canopy shadows or multiple scattering (Chen and Leblanc, 2001), particularly at high-resolution scales. In terms of retrieval scale, our research is designed to achieve spatially continuous pixel-to-pixel LCC retrieval, distinguishing from the past focus on individual tree scales, which typically allows for a more precise concentration of signals on the tree canopy and, consequently, more accurate parameter retrieval (Cheng et al., 2022). The shift to pixel-scale retrieval exposes each pixel's reflectance to greater susceptibility to interference from the surroundings, which is a contributing factor to the reduced accuracy observed in our LCC retrieval efforts.

In addition to the influence of these factors, the structural attributes of the plots and the positions of leaf collection in the field also require careful consideration. Field measurements reveal that the Larch and Spruce plots exhibit canopy coverages of 0.62 and 0.42, respectively. Plots with lower canopy coverage expose a greater amount of soil, which in turn introduces increased soil interference into pixel reflectance (Li et al., 2023) and consequently diminishes the precision of LCC retrieval. Which also is consistent with the results observed in our study, clearly showing that LCC retrieval accuracy is higher in the Larch plots compared to the Spruce plots. In terms of leaf collection positions, particularly for the Larch plots, the LCC retrieval results were found to be lower than the corresponding field measurements. This discrepancy primarily stems from the limited collection of leaves from the upper canopy regions, which is often hindered by sampling difficulties. However, a large proportion of UAV signals are derived from the upper canopy layers. Previous studies have shown that vegetation chlorophyll content varies in a gradient from low to high from canopy top to canopy bottom, enabling shaded leaves to absorb more sunlight for their own growth (Shen et al., 2020). Therefore, this leads to an underestimation of LCC in the Larch plots.

4.2. 3D RT vs 1D RT for LCC retrieval

In this study, we primarily utilized the 3D Semi-LESS and 1D PROSAIL models to simulate UAV reflectance data for generating training datasets, which were then input to a 1D residual neural network trained for LCC retrieval. Overall, both simulated theoretical test datasets (Table 4) and field-measured data indicate that the Semi-LESS model (Fig. 10) outperforms the PROSAIL model (Fig. 11) in terms of LCC retrieval accuracy. The superior performance of the Semi-LESS model in LCC retrieval is primarily attributed to its ability to finely depict the complex interactions between solar radiation and the heterogeneous forest canopy. During the simulation of signals, we also leveraged the model's utilization of high-resolution structural data. By employing precise structural information obtained from UAV LiDAR point clouds, we conducted a detailed reconstruction of forest structural scenes. The incorporation of this a priori knowledge also enabled the calibration of

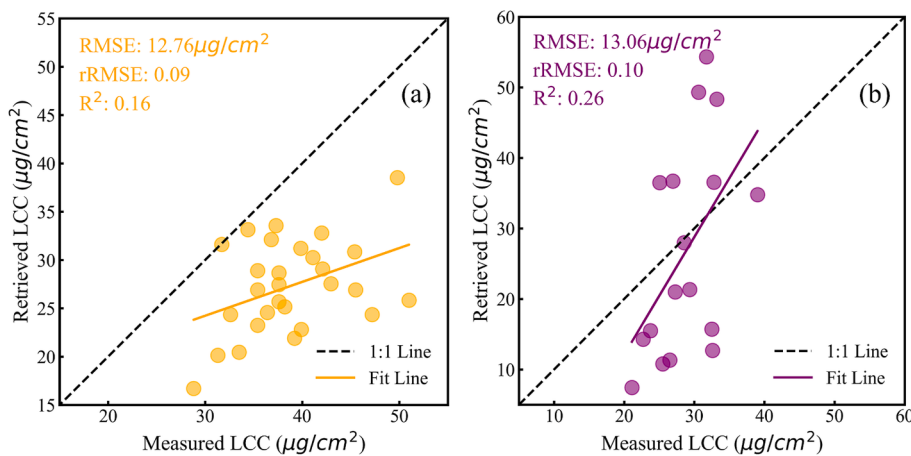


Fig. 11. Comparison of LCC retrieval accuracy by residual networks in the Larch (a) and Spruce (b) plot (Residual networks trained based on the PROSAIL dataset).

the Semi-LESS model to simulate real UAV reflectance for corresponding plots. Previous studies have indicated that introducing a priori knowledge can reduce biases in model-simulated reflectance and further enhance the model's inversion accuracy (Xu et al., 2019). In contrast, PROSAIL's simplification of the canopy as a homogeneous layer overlooks canopy heterogeneity that can lead to biases in simulated reflectance. Despite calibrating the PROSAIL model with the plant area index (PAI) derived from UAV LiDAR point clouds, additional factors such as canopy shape and distribution can still introduce errors in UAV signal simulations (Croft et al., 2013).

On the other hand, the Semi-LESS model fully leverages the advantages of high-resolution imagery, simulating image datasets that match the spatial resolution of observed UAV imagery. It further selects sunlit pixels through near-infrared reflectance thresholds to generate training datasets, thereby also reducing interference from background elements such as shadows in LCC retrieval. In contrast, the PROSAIL model struggles to interpret and utilize signals from high-resolution imagery. Ultimately, the Semi-LESS model, with its interpretable processes, enables the rapid generation of a substantial amount of training data for neural network training, similar to the PROSAIL model. This capability allows the model to meet the precision management needs of the agroforestry sectors for vegetation.

4.3. Impact of shadows

Shadows, integral components of vegetation canopies, are predominantly shaped by canopy architecture and the interplay of sun-sensor geometry (Zeng et al., 2023). In this study, for the UAV image dataset simulated by the Semi-LESS model, we utilized 25 % near-infrared reflectance as a criterion to differentiate between sunlit and shaded pixels in UAV imagery, and only sunlit pixels were aggregated for LCC retrieval. Previous studies have demonstrated that shadows have a significant impact on the reflectance of vegetation canopies, leading to considerable uncertainty in accurately retrieving leaf biochemical properties and pigment composition (Jiang et al., 2019; Zeng et al., 2023). Moreover, our theoretical simulation data and field-measured data results show that the accuracy of LCC retrieval, when aggregating only sunlit pixels, is superior to that achieved by aggregating a mixture of shaded and sunlit pixels. This enhancement is primarily due to the increased signal-to-noise ratio of the reflectance per pixel after the exclusion of shaded pixels. Specifically, in some chlorophyll-sensitive bands, such as the green band, there is a pronounced absorption peak, and the slope from the red edge to the near-infrared band increases (Fig. 8). Previous studies have also indicated that excluding the effects of shadows in high-resolution imagery can enhance the accuracy of chlorophyll retrieval (Ferreira et al., 2018; Zhang et al., 2024), and our findings are consistent with these prior investigations.

4.4. Advantages and limitations

In this process, detailed 3D forest structural scenes, reconstructed from high-resolution UAV LiDAR point clouds, are input into the Semi-LESS model to ensure precise structural scene representation, which is crucial for reducing biases in UAV-simulated reflectance. The model's analytical capabilities also enhance the efficiency of UAV signal simulation. These advantages are key to our subsequent use of deep learning for retrieving fine-scale LCC. However, when reconstructing forest scenes with UAV LiDAR point clouds, the intermixture of branch and leaf point clouds often hinders the clear separation of these components. Previous studies have indicated that woody elements can influence the spectral response, which in turn can affect the estimation of chlorophyll content (Cheng et al., 2022). Therefore, conducting a clear separation of branch and leaf point clouds based on UAV point clouds (Cai et al., 2024) are crucial for reducing this uncertainty in LCC retrieval. Additionally, based on previous research, Leaf Area Index (LAI) is another significant interference factor in LCC retrieval. Although we utilized ALS

point clouds combined with a path length distribution algorithm (Gao et al., 2023) to estimate PAI for sub-canopy parameterization, further exploration is needed to understand the biases in PAI estimation algorithms and the co-variance between PAI and LCC (Li et al., 2021), both of which impact LCC retrieval. Besides these, leaf angle distribution and leaf clumping effects also deserve further attention (Cheng et al., 2023).

5. Conclusion

We utilized the semi-empirically accelerated 3D radiative transfer model, Semi-LESS, coupled with a 1D residual network, to conduct fine-scale retrieval of LCC from UAV imagery and LiDAR point clouds. To enhance the accuracy of LCC retrieval, shadow information was explicitly excluded from the simulated UAV imagery. Furthermore, to assess the comparative capabilities of the 1D PROSAIL and 3D Semi-LESS model in retrieving LCC parameters. Theoretical simulation datasets and field-measured data from two selected plots were utilized to assess the accuracy of the model in retrieving LCC parameters. Specifically, for the Larch plot, the accuracy of LCC retrieval for measured and simulated data before shadow exclusion was $R^2 = 0.33\text{--}0.87$, $RMSE = 10.68 \mu\text{g}/\text{cm}^2\text{--}6.7 \mu\text{g}/\text{cm}^2$, and $rRMSE = 0.07\text{--}0.001$; after shadow exclusion, it improved to $R^2 = 0.42\text{--}0.91$, $RMSE = 8.21 \mu\text{g}/\text{cm}^2\text{--}5.4 \mu\text{g}/\text{cm}^2$, and $rRMSE = 0.05\text{--}0.001$. Similarly, in the Spruce plot, the accuracy before shadow exclusion was $R^2 = 0.29\text{--}0.76$, $RMSE = 11.51 \mu\text{g}/\text{cm}^2\text{--}9.08 \mu\text{g}/\text{cm}^2$, and $rRMSE = 0.1\text{--}0.003$; after shadow exclusion, it improved to $R^2 = 0.33\text{--}0.86$, $RMSE = 9.76 \mu\text{g}/\text{cm}^2\text{--}6.92 \mu\text{g}/\text{cm}^2$, and $rRMSE = 0.09\text{--}0.002$. When comparing different radiative transfer models, the results from both plots indicate that the accuracy of LCC retrieval using the Semi-LESS model is higher than that of the PROSAIL model. Specifically, in the case of Larch plot, the PROSAIL model's accuracy was $R^2 = 0.16\text{--}0.81$, $RMSE = 12.76 \mu\text{g}/\text{cm}^2\text{--}7.76 \mu\text{g}/\text{cm}^2$, and $rRMSE = 0.09\text{--}0.001$; in the case of Spruce plot, it was $R^2 = 0.26\text{--}0.70$, $RMSE = 13.06 \mu\text{g}/\text{cm}^2\text{--}9.83 \mu\text{g}/\text{cm}^2$, and $rRMSE = 0.1\text{--}0.004$. Our results demonstrate that coupling the Semi-LESS model with deep learning enables fine-scale LCC retrieval and highlights the importance of addressing shadows in fine-scale LCC retrieval.

CRediT authorship contribution statement

Xun Zhao: Writing – review & editing, Writing – original draft, Visualization, Validation, Software, Methodology, Investigation, Data curation, Conceptualization. **Jianbo Qi:** Writing – review & editing, Supervision, Resources, Methodology, Funding acquisition, Conceptualization. **Jingyi Jiang:** Conceptualization. **Shangbo Liu:** Visualization, Validation, Investigation. **Haifeng Xu:** Visualization, Software, Methodology. **Simei Lin:** Writing – review & editing, Investigation. **Zhexiu Yu:** Writing – review & editing, Visualization. **Linyuan Li:** Writing – review & editing, Investigation. **Huaguo Huang:** Supervision.

Declaration of competing interest

The authors declare that they have no known competing financial interests or personal relationships that could have appeared to influence the work reported in this paper.

Acknowledgements

This work was supported by the National Natural Science Foundation of China (Grant No. 42371345), Beijing Nova Program (20240484556) and Fundamental Research Funds for the Central Universities (2233300001).

Data availability

Data will be made available on request.

References

- Bailey, B.N., 2014. A scalable plant-resolving radiative transfer model based on optimized GPU ray tracing. *Agricultural and Forest Meteorology* 17.
- Bhadra, S., Sagan, V., Sarkar, S., Braud, M., Mockler, T.C., Eveland, A.L., 2024. PROSAIL-net: a transfer learning-based dual stream neural network to estimate leaf chlorophyll and leaf angle of crops from UAV hyperspectral images. *ISPRS J. Photogramm. Remote Sens.* 210, 1–24. <https://doi.org/10.1016/j.isprsjprs.2024.02.020>.
- Bian, Z., Wu, S., Roujean, J.-L., Cao, B., Li, H., Yin, G., Du, Y., Xiao, Q., Liu, Q., 2022. A TIR forest reflectance and transmittance (FRT) model for directional temperatures with structural and thermal stratification. *Remote Sens. Environ.* 268, 112749. <https://doi.org/10.1016/j.rse.2021.112749>.
- Cai, S., Zhang, W., Zhang, S., Yu, S., Liang, X., 2024. Branch architecture quantification of large-scale coniferous forest plots using UAV-LiDAR data. *Remote Sens. Environ.* 306, 114121. <https://doi.org/10.1016/j.rse.2024.114121>.
- Chen, J.M., Leblanc, S.G., 2001. Multiple-scattering scheme useful for geometric optical modeling. *IEEE Trans. Geosci. Remote Sens.* 39, 1061–1071. <https://doi.org/10.1109/36.921424>.
- Chen, R., Liu, W., Yang, H., Jin, X., Yang, G., Zhou, Y., Zhang, C., Han, S., Meng, Y., Zhai, C., Feng, H., 2024. A novel framework to assess apple leaf nitrogen content: fusion of hyperspectral reflectance and phenology information through deep learning. *Comput. Electron. Agric.* 219, 108816. <https://doi.org/10.1016/j.compag.2024.108816>.
- Cheng, J., Yang, H., Qi, J., Sun, Z., Han, S., Feng, H., Jiang, J., Xu, W., Li, Z., Yang, G., Zhao, C., 2022. Estimating canopy-scale chlorophyll content in apple orchards using a 3D radiative transfer model and UAV multispectral imagery. *Comput. Electron. Agric.* 202, 107401. <https://doi.org/10.1016/j.compag.2022.107401>.
- Cheng, J., Yang, H., Qi, J., Han, S., Sun, Z., Feng, H., Chen, R., Zhang, C., Li, J., Yang, G., 2023. Evaluation of the effect of leaf spatial aggregation on chlorophyll content retrieval in open-canopy apple orchards. *Int. J. Appl. Earth Obs. Geoinf.* 121, 103367. <https://doi.org/10.1016/j.jag.2023.103367>.
- Coops, N.C., Tompalski, P., Goodbody, T.R.H., Queinnec, M., Luther, J.E., Bolton, D.K., White, J.C., Wulder, M.A., van Lier, O.R., Hermosilla, T., 2021. Modelling lidar-derived estimates of forest attributes over space and time: A review of approaches and future trends. *Remote Sens. Environ.* 260, 112477. <https://doi.org/10.1016/j.rse.2021.112477>.
- Croft, H., Chen, J.M., Zhang, Y., Simic, A., 2013. Modelling leaf chlorophyll content in broadleaf and needle leaf canopies from ground, CASI, Landsat TM 5 and MERIS reflectance data. *Remote Sens. Environ.* 133, 128–140. <https://doi.org/10.1016/j.rse.2013.02.006>.
- Croft, H., Chen, J.M., Wang, R., Mo, G., Luo, S., Luo, X., He, L., Gonsamo, A., Arabian, J., Zhang, Y., Simic-Milas, A., Noland, T.L., He, Y., Homolová, L., Malenovský, Z., Yi, Q., Beringer, J., Amiri, R., Huttley, L., Arellano, P., Stahl, C., Bonal, D., 2020. The global distribution of leaf chlorophyll content. *Remote Sens. Environ.* 236, 111479. <https://doi.org/10.1016/j.rse.2019.111479>.
- Edelsbrunner, H., Mücke, E.P., 1994. Three-dimensional alpha shapes, in: Proceedings of the 1992 Workshop on Volume Visualization, VVS '92. Association for Computing Machinery, New York, NY, USA, pp. 75–82. doi: 10.1145/147130.147153.
- Feret, J.-B., François, C., Asner, G.P., Gitelson, A.A., Martin, R.E., Bidé, L.P.R., Ustin, S. L., Le Maire, G., Jacquemoud, S., 2008. PROSPECT-4 and 5: Advances in the leaf optical properties model separating photosynthetic pigments. *Remote Sens. Environ.* 112, 3030–3043. <https://doi.org/10.1016/j.rse.2008.02.012>.
- Ferreira, M.P., Feret, J.-B., Grau, E., Gastellu-Etchegorry, J.-P., Shimabukuro, Y.E., de Souza Filho, C.R., 2018. Retrieving structural and chemical properties of individual tree crowns in a highly diverse tropical forest with 3D radiative transfer modeling and imaging spectroscopy. *Remote Sens. Environ.* 211, 276–291. <https://doi.org/10.1016/j.rse.2018.04.023>.
- Gao, G., Qi, J., Lin, S., Hu, R., Huang, H., 2023. Estimating plant area density of individual trees from discrete airborne laser scanning data using intensity information and path length distribution. *Int. J. Appl. Earth Obs. Geoinf.* 118, 103281. <https://doi.org/10.1016/j.jag.2023.103281>.
- Gastellu-Etchegorry, J.P., Martin, E., Gascon, F., 2004. DART: a 3D model for simulating satellite images and studying surface radiation budget. *Int. J. Remote Sens.* 25, 73–96. <https://doi.org/10.1080/0143116031000115166>.
- Gressin, A., Mallet, C., Demantké, J., David, N., 2013. Towards 3D lidar point cloud registration improvement using optimal neighborhood knowledge. *ISPRS J. Photogramm. Remote Sens.* 79, 240–251. <https://doi.org/10.1016/j.isprsjprs.2013.02.019>.
- He, S., Qi, J., Wang, D., Yan, K., Huang, H., 2024. Estimation of canopy photon recollision probability from airborne laser scanning. *Remote Sens. Environ.* 311, 114264. <https://doi.org/10.1016/j.rse.2024.114264>.
- Houborg, R., Anderson, M.C., Daughtry, C.S.T., Kustas, W.P., Rodell, M., 2011. Using leaf chlorophyll to parameterize light-use-efficiency within a thermal-based carbon, water and energy exchange model. *Remote Sens. Environ.* 115, 1694–1705. <https://doi.org/10.1016/j.rse.2011.02.027>.
- Huang, H., Qin, W., Liu, Q., 2013. RAPID: A Radiosity Applicable to Porous Individual Objects for directional reflectance over complex vegetated scenes. *Remote Sens. Environ.* 132, 221–237. <https://doi.org/10.1016/j.rse.2013.01.013>.
- Jacquemoud, S., Verhoef, W., Baret, F., Bacour, C., Zarco-Tejada, P.J., Asner, G.P., François, C., Ustin, S.L., 2009. PROSPECT+SAIL models: A review of use for vegetation characterization. *Remote Sens. Environ. Imaging Spectr. Special Issue* 113, S56–S66. <https://doi.org/10.1016/j.rse.2008.01.026>.
- Jiang, C., Fang, H., 2019. GSV: a general model for hyperspectral soil reflectance simulation. *Int. J. Appl. Earth Obs. Geoinf.* 83, 101932. <https://doi.org/10.1016/j.jag.2019.101932>.
- Jiang, H., Wang, S., Cao, X., Yang, C., Zhang, Z., Wang, X., 2019. A shadow-eliminated vegetation index (SEVI) for removal of self and cast shadow effects on vegetation in rugged terrains. *Int. J. Digital Earth* 12, 1013–1029. <https://doi.org/10.1080/17538947.2018.1495770>.
- Jiang, J., Weiss, M., Liu, S., Rochdi, N., Baret, F., 2020. Speeding up 3D radiative transfer simulations: A physically based metamodel of canopy reflectance dependency on wavelength, leaf biochemical composition and soil reflectance. *Remote Sens. Environ.* 237, 111614. <https://doi.org/10.1016/j.rse.2019.111614>.
- Kira, O., Linker, R., Gitelson, A., 2015. Non-destructive estimation of foliar chlorophyll and carotenoid contents: Focus on informative spectral bands. *Int. J. Appl. Earth Obs. Geoinf.* 38, 251–260. <https://doi.org/10.1016/j.jag.2015.01.003>.
- Li, D., Chen, J.M., Yu, W., Zheng, H., Yao, X., Cao, W., Wei, D., Xiao, C., Zhu, Y., Cheng, T., 2022. Assessing a soil-removed semi-empirical model for estimating leaf chlorophyll content. *Remote Sens. Environ.* 282, 113284. <https://doi.org/10.1016/j.rse.2022.113284>.
- Li, W., Guo, Q., Tao, S., Su, Y., 2018. VBRT: a novel voxel-based radiative transfer model for heterogeneous three-dimensional forest scenes. *Remote Sens. Environ.* 206, 318–335. <https://doi.org/10.1016/j.rse.2017.12.043>.
- Li, Y., Ma, Q., Chen, J.M., Croft, H., Luo, X., Zheng, T., Rogers, C., Liu, J., 2021. Fine-scale leaf chlorophyll distribution across a deciduous forest through two-step model inversion from Sentinel-2 data. *Remote Sens. Environ.* 264, 112618. <https://doi.org/10.1016/j.rse.2021.112618>.
- Li, L., Mu, X., Jiang, H., Chianucci, F., Hu, R., Song, W., Qi, J., Liu, S., Zhou, J., Chen, L., Huang, H., Yan, G., 2023. Review of ground and aerial methods for vegetation cover fraction (fCover) and related quantities estimation: definitions, advances, challenges, and future perspectives. *ISPRS J. Photogramm. Remote Sens.* 199, 133–156. <https://doi.org/10.1016/j.isprsjprs.2023.03.020>.
- Lin, S., Li, L., Liu, S., Gao, G., Zhao, X., Chen, L., Qi, J., Shen, Q., Huang, H., 2024. Stratified burn severity assessment by integrating spaceborne spectral and waveform attributes in great xing'an mountain. *Remote Sens. Environ.* 307, 114152. <https://doi.org/10.1016/j.rse.2024.114152>.
- Liu, W., Atherton, J., Mottus, M., Gastellu-Etchegorry, J.-P., Malenovsky, Z., Raunonen, P., Akerblom, M., Makipaa, R., Porcar-Castell, A., 2019. Simulating solar-induced chlorophyll fluorescence in a boreal forest stand reconstructed from terrestrial laser scanning measurements. *Remote Sens. Environ.* 232, 111274. <https://doi.org/10.1016/j.rse.2019.111274>.
- Makhlofi, A., Kallel, A., 2023. Inversion of a New designed ANN-based 3-D-RTM Emulator by continuous MCMC technique to monitor crop biophysical properties using sentinel-2 images. *IEEE Trans. Geosci. Remote Sens.* 61, 1–14. <https://doi.org/10.1109/TGRS.2023.3297363>.
- North, P.R.J., 1996. Three-dimensional forest light interaction model using a monte carlo method. *IEEE Trans. Geosci. Remote Sens.* 34, 946–956. <https://doi.org/10.1109/36.508411>.
- Qi, J., Xie, D., Guo, D., Yan, G., 2017. A large-scale emulation system for realistic three-dimensional (3-D) forest simulation. *IEEE J. Sel. Top. Appl. Earth Obs. Remote Sens.* 10, 4834–4843. <https://doi.org/10.1109/JSTARS.2017.2714423>.
- Qi, J., Xie, D., Yin, T., Yan, G., Gastellu-Etchegorry, J.-P., Li, L., Zhang, W., Mu, X., Norford, L.K., 2019. LESS: Large-Scale remote sensing data and image simulation framework over heterogeneous 3D scenes. *Remote Sens. Environ.* 221, 695–706. <https://doi.org/10.1016/j.rse.2018.11.036>.
- Qi, J., Xie, D., Jiang, J., Huang, H., 2022. 3D radiative transfer modeling of structurally complex forest canopies through a lightweight boundary-based description of leaf clusters. *Remote Sens. Environ.* 283, 113301. <https://doi.org/10.1016/j.rse.2022.113301>.
- Qi, J., Jiang, J., Zhou, K., Xie, D., Huang, H., 2023. Fast and accurate simulation of canopy reflectance under wavelength-dependent optical properties using a semi-empirical 3D radiative transfer model. *J. Remote Sens.* 3, 0017. <https://doi.org/10.34133/remotesensing.0017>.
- Shen, X., Cao, L., Coops, N.C., Fan, H., Wu, X., Liu, H., Wang, G., Cao, F., 2020. Quantifying vertical profiles of biochemical traits for forest plantation species using advanced remote sensing approaches. *Remote Sens. Environ.* 250, 112041. <https://doi.org/10.1016/j.rse.2020.112041>.
- Verhoef, W., 1984. Light scattering by leaf layers with application to canopy reflectance modeling: The SAIL model. *Remote Sens. Environ.* 16, 125–141. [https://doi.org/10.1016/0034-4257\(84\)90057-9](https://doi.org/10.1016/0034-4257(84)90057-9).
- Widlowski, J.-L., Mio, C., Disney, M., Adams, J., Andredakis, I., Atzberger, C., Brennan, J., Busetto, L., Chelle, M., Ceccherini, G., Colombo, R., Côté, J.-F., Eenmäe, A., Essery, R., Gastellu-Etchegorry, J.-P., Gobron, N., Grau, E., Haverd, V., Homolová, L., Huang, H., Hunt, L., Kobayashi, H., Koetz, B., Kuusk, A., Kuusk, J., Lang, M., Lewis, P.E., Lovell, J.L., Malenovský, Z., Meroni, M., Morsdorf, F., Möttus, M., Ni-Meister, W., Pinty, B., Rautiainen, M., Schlerf, M., Somers, B., Stuckens, J., Verstraete, M.M., Yang, W., Zhao, F., Zenone, T., 2015. The fourth phase of the radiative transfer model intercomparison (RAMI) exercise: Actual canopy scenarios and conformity testing. *Remote Sens. Environ.* 169, 418–437. <https://doi.org/10.1016/j.rse.2015.08.016>.
- Xu, Z., He, A., Zhang, Y., Hao, Z., Li, Y., Xiang, S., Li, B., Chen, L., Yu, H., Shen, W., Huang, X., Guo, X., Li, Z., 2023. Retrieving chlorophyll content and equivalent water thickness of moso bamboo (*phyllostachys pubescens*) forests under *pantana phyllostachys* chao-induced stress from sentinel-2A/B images in a multiple LUTs-based PROSAIL framework. *For. Ecosyst.* 10, 100108. <https://doi.org/10.1016/j.forecosys.2023.100108>.
- Xu, M., Liu, R., Chen, J.M., Liu, Y., Shang, R., Ju, W., Wu, C., Huang, W., 2019. Retrieving leaf chlorophyll content using a matrix-based vegetation index combination approach. *Remote Sens. Environ.* 224, 60–73. <https://doi.org/10.1016/j.rse.2019.01.039>.

- Xu, Lu, J.S., Zhang, N., Yang, T.C., He, J.Y., Yao, X., Cheng, T., Zhu, Y., Cao, W.X., Tian, Y.C., 2019. Inversion of rice canopy chlorophyll content and leaf area index based on coupling of radiative transfer and Bayesian network models. *ISPRS J. Photogramm. Remote Sens.* 150, 185–196. <https://doi.org/10.1016/j.isprsjprs.2019.02.013>.
- Zeng, Y., Hao, D., Park, T., Zhu, P., Huete, A., Myneni, R., Knyazikhin, Y., Qi, J., Nemani, R.R., Li, F., Huang, J., Gao, Y., Li, B., Ji, F., Köhler, P., Frankenber, C., Berry, J.A., Chen, M., 2023. Structural complexity biases vegetation greenness measures. *Nat. Ecol. Evol.* 7, 1790–1798. <https://doi.org/10.1038/s41559-023-02187-6>.
- Zhang, C., Chen, Z., Yang, G., Xu, B., Feng, H., Chen, R., Qi, N., Zhang, W., Zhao, D., Cheng, J., Yang, H., 2024. Removal of canopy shadows improved retrieval accuracy of individual apple tree crowns LAI and chlorophyll content using UAV multispectral imagery and PROSAIL model. *Comput. Electron. Agric.* 221, 108959. <https://doi.org/10.1016/j.compag.2024.108959>.
- Zhang, W., Qi, J., Wan, P., Wang, H., Xie, D., Wang, X., Yan, G., 2016. An easy-to-use airborne LiDAR data filtering method based on cloth simulation. *Remote Sens. (Basel)* 8, 501. <https://doi.org/10.3390/rs8060501>.
- Zhao, X., Qi, J., Xu, H., Yu, Z., Yuan, L., Chen, Y., Huang, H., 2023. Evaluating the potential of airborne hyperspectral LiDAR for assessing forest insects and diseases with 3D Radiative Transfer Modeling. *Remote Sens. Environ.* 297, 113759. <https://doi.org/10.1016/j.rse.2023.113759>.
- Zhao, X., Qi, J., Yu, Z., Yuan, L., Huang, H., 2024. Fine-scale quantification of absorbed photosynthetically active radiation (APAR) in plantation forests with 3D radiative transfer modeling and LiDAR data. *Plant Phenomics* 6, 166. <https://doi.org/10.34133/plantphenomics.0166>.